FINAL TECHNICAL REPORT

Award #03HQGR0085

SOURCE RUPTURE PROCESS OF THE 1971 SAN FERNANDO EARTHQUAKE: COLLABORATIVE RESEACH WITH URS AND USGS

Robert Graves
URS Group Inc.
566 El Dorado Stree, 2nd Floor
Pasadena, CA 91101

Tel: 626-449-7650
Fax: 626-449-3536
Email: Robert_graves@urscorp.com

FINAL TECHNICAL REPORT

Award #03HQGR0085

SOURCE RUPTURE PROCESS OF THE 1971 SAN FERNANDO EARTHQUAKE: COLLABORATIVE RESEACH WITH URS AND USGS

Robert Graves
URS Group Inc.
566 El Dorado Stree, 2nd Floor
Pasadena, CA 91101

Tel: 626-449-7650
Fax: 626-449-3536
Email: Robert_graves@urscorp.com

Abstract

The 1971 San Fernando earthquake is the only thrust event producing significant surface rupture to be widely recorded in Southern California. Numerous important studies of this event have been conducted over the years, and collectively, they provide a strong foundation for understanding the overall characteristics of this earthquake. Our original goal in this project is to develope a kinematic rupture model of the San Fernando earthquake using a joint inversion methodology. This methodology attempts to simultaneously satisfy multiple (complementary) datasets, including teleseismic, strong motion, geodetic, and geologic observations. Each of these datasets is sensitive to different characteristics of the rupture process and the joint inversion methodology provides a formal approach to integrate these observations into a single, comprehensive rupture model. After collecting some of the ground motion data, we quickly realized that the complex 3D geologic structure of the San Fernando basin had a significant impact on the ground response, both for the strong motion waveforms, as well as the geodetic displacements. Based on our previous studies of these 3D effects on source inversion studies (Graves and Wald, 2001; Wald and Graves, 2001; Awards #1434-HQ-97-GR03023 and #99HQGR0088), we decided to concentrate our efforts first on developing a better understanding of how well ground motion waveforms can be modeled in a 3D velocity structure. The goal of this work is to develop a framework for assessing the accuracy of the 3D Green's functions (and the underlying velocity structure) as a function of frequency, in order to then determine the appropriate bandwidth over which this 3D velocity model can be used for source inversion studies. For this study, we selected a moderated-sized event that was well recorded throughout a basin structure environment.

The 2001 Big Bear Lake earthquake (M_w 4.63) was recorded by over 30 strong motion instruments in the San Bernardino basin region of Southern California. At periods longer than about 1 second, the ground motions in the central portion of the basin have significantly larger amplitudes and extended durations of strong shaking relative to sites outside the basin. In many cases, the peak motions at the basin sites occur 10 or more seconds after the direct S-wave arrival, suggesting that these motions are controlled by basin-generated surface waves. To

model these motions, I have performed numerical wave field simulations using a 3D representation of the basin velocity structure and a point double-couple representation of the earthquake source. The basin model is derived from potential field data and has been used previously for modeling the long period (T > 3 sec) response of the Hector Mine earthquake. It is characterized by low velocity sediment accumulations that are relatively thin in the northern portion of the basin adjacent to the San Andreas fault, and then steadily increase in thickness toward the south, reaching a maximum thickness of about 1.8 km just north of the San Jacinto fault. In modeling the Big Bear Lake earthquake, I use a minimum shear velocity of 250 m/s, which yields a bandwidth resolution limit of T > 1 sec for the numerical simulations at a grid spacing of 50 m. The results of the simulation for the Big Bear Lake earthquake using the current model do quite well at reproducing the observed waveforms, amplitudes and durations at periods of 3 sec and longer throughout the San Bernardino basin region. At shorter periods (1 – 2 secs), the fit to the recorded motions is less well resolved, particularly in terms of deterministically matching the waveforms of the later arriving phases. This suggests that extending the modeling down to periods near 1 second represents a more complex task than simply reducing the minimum velocity threshold in the numerical calculation, and in particular, requires detailed knowledge of the subsurface structure and distribution of seismic velocities at relatively short length scales (on the order of 50 m). Furthermore, these results indicate that structural complexity at non-basin sites becomes increasingly important as we attempt to model shorter period motions, and its effects on the propagating wave field must be considered in addition to the basin structure response.

The Seismic Response of the San Bernardino Basin Region during the 2001 Big Bear Lake Earthquake

Robert W. Graves
URS Corporation
566 El Dorado St.
Pasadena, CA 91101

robert_graves@urscorp.com

submitted to: *Bulletin of Seismological Society of America*
December 21, 2006

Abstract

The 2001 Big Bear Lake earthquake (M_w 4.63) was recorded by over 30 strong motion instruments in the San Bernardino basin region of Southern California. At periods longer than about 1 second, the ground motions in the central portion of the basin have significantly larger amplitudes and extended durations of strong shaking relative to sites outside the basin. In many cases, the peak motions at the basin sites occur 10 or more seconds after the direct S-wave arrival, suggesting that these arrivals are controlled by basin-generated surface waves. To model these motions, I have performed finite-difference simulations using a 3D representation of the basin velocity structure. The basin structure has a minimum shear velocity of 250 m/s, which coupled with the model grid spacing of 50 m yields a bandwidth resolution limit of T > 1 sec for the numerical simulations. The simulations do quite well at reproducing the observed waveforms,

amplitudes and durations at periods of 3 sec and longer. At shorter periods (1 – 2 secs), the fit to the recorded motions is less well resolved, especially in matching the waveforms of the later arriving phases. This suggests that in regions of complex geology, deterministic waveform modeling at periods approaching 1 second involves more than simply reducing the minimum velocity threshold, and in particular, requires knowledge of the subsurface structure and distribution of seismic velocities at relatively short length scales (on the order of 50 m).

Introduction

Graves and Wald (2004) recently studied the long-period ground motion response of the San Bernardino basin region during the 1999 M_w 7.1 Hector Mine earthquake. They found significant ground motion amplification and extended durations of strong shaking at sites located over the deep sediments of the central basin. In addition, they showed that these data could be modeled reasonably well using a 3D velocity structure characterized by a gently southwestward dipping basement interface that reaches its maximum depth just north of the San Jacinto fault. Due to the dominance of longer period energy in the Hector Mine earthquake (see Boore et al., 2002), and computational limitations of the simulation model, the Graves and Wald (2004) analysis was primarily restricted to periods of about 3 seconds and longer.

Analysis of the shorter period (around 1 sec) basin response in the San Bernardino region was first performed by Frankel (1994) using aftershocks of the 1992 Landers / Big Bear earthquake sequence recorded on temporary instrument arrays. The data were obtained on three tripartite arrays, two situated on the basin sediments and one on a nearby rock site. He found significant amplification of motions and much longer durations of shaking at the basin sites relative to the rock site. In addition, array analysis of the waveform data showed that the later-arriving phases are dominated by surface waves propagating in various directions across the basin. Using a relatively simple 3D velocity model, he was able to reproduce the general characteristics of these data. The main limitations of the Frankel (1994) study were

that the instrument arrays only sampled the basin response at two locations, the bandwidth of the recordings was restricted due to the instrumentation and small event magnitudes (M < 3), and the small magnitudes precluded determination of robust source mechanism information.

In the current work, I build on these previous studies through the analysis and 3D simulation of ground motion data from the 2001 M_w 4.63 Big Bear Lake earthquake. This event was recorded at numerous digital strong motion sites, including about 20 sites within the San Bernardino basin (see Figure 1). The magnitude of this event is large enough to generate significant energy at the mid-period range (1-5 seconds), yet small enough so that source process is relatively simple in this bandwidth. These characteristics allow for a more detailed analysis of the ground motion response than was possible in the earlier studies.

In the sections that follow, I first discuss the characteristics of the observed ground motions for this event in the San Bernardino basin region. I then provide a review of the regional 3D velocity structure, including modifications made to the earlier model for the current set of simulations. This is followed by a detailed discussion of the ground motion simulations for the Big Bear Lake earthquake, along with a comprehensive comparison of the synthetic and recorded waveforms at both basin and non-basin sites. I conclude with a discussion of the factors that are currently limiting our ability to deterministically model the recorded waveforms at shorter periods (~ 1 sec), as well as the implications of these modeling results for estimating ground motion waveforms for future earthquakes in this region.

Observed Ground Motions

The M_w 4.63 Big Bear Lake earthquake occurred on 02/10/01 at a depth of 7.5 km just north of the San Bernardino region of southern California. The mechanism of the event is primarily strike-slip (Table 1) as determined by regional waveform inversion (e.g., Zhu and Helmberger, 1996). Ground motion

waveforms were recorded at nearly 30 stations in and around the San Bernardino basin region. These stations are part of the Southern California Seismic Network (SCSN) operated jointly by the US Geological Survey (USGS) and Caltech, and the California Strong Motion Instrumentation Program (CSMIP) operated by the California Geological Survey (CGS). The waveform data are available from the Cosmos Virtual Data Center (http://db.cosmos-eq.org). Table 2 lists the station locations and the passband of the recorded time histories. For the Caltech and USGS data, I obtained the uncorrected time histories and applied a fourth-order, zero-phase butterworth filter with corners at 0.04 and 10 sec. The CGS data were only distributed as corrected time histories, and were processed by CGS using a standard small event filter with corners at 0.025 and 3 sec. Figure 1 shows the distribution of the strong motion stations and the event epicenter. Note that there is a large concentration of stations within the San Bernardino basin, which lies in the wedge shaped region between the San Andreas and San Jacinto faults.

Figure 2 displays profiles of the recorded ground motion time histories rotated to tangential and radial components relative to the epicenter. For these profiles, I have integrated the recorded accelerations to ground velocity. Figure 2a displays the broadband motions (passband given in Table 2) and Figure 2b displays the motions filtered in the passband T > 1 sec. The plotting sequence of the stations in these profiles is roughly with increasing epicentral distance. Thus, the stations at the top of the profiles are located closest to the epicenter, generally along the northern margin of the San Bernardino basin, the stations in the middle of the profiles are located within the central basin (indicated by the large brackets), and the stations at the bottom of the profiles are located furthest from the epicenter, generally south and west of the basin.

The motions at the sites along the northern margin of the basin are characterized by relatively short durations (less than about 5 sec) with the peak motions primarily being controlled by the direct S wave. One interesting facet of these data is that the broadband ground velocities (Figure 2a) show significant variability between closely located sites, for example stations **5336** and **5161**. These ground motion

differences are likely the result of differences in the fine-scale near-surface geologic structure at these sites, which primarily affects the shorter period response (T < 1 sec). The filtered (T > 1 sec) motions shown in Figure 2b exhibit much more similarity in waveform and amplitude at these two sites, indicating that the source and path are the main factors controlling the longer period ground motion response. Another interesting characteristic of the longer period (T > 1 sec) motions is that even though these sites are located outside of the deep basin region (i.e., non-basin sites), there is still complexity in the observed waveforms.

The stations located within the central basin region clearly show amplified motions and extended durations of shaking relative to the sites outside of the basin. This is true in both the broadband records and the low-pass filtered records. In addition, for many of the basin sites the largest motions occur later in the records after the direct arrivals. This is particularly apparent for the lower frequency motions (Figure 2b), suggesting the influence of deeper geologic structure as opposed to near-surface site response effects. These types of ground motion characteristics are indicative of basin response effects such as the generation and propagation of basin surface waves.

The motions at stations south and west of the basin (e.g., **5330**, **2388**, **fon**, **rvr**) have noticeably lower amplitudes than the nearby basin sites. This is particularly true for the later arriving phases. In many respects, the motions at these sites are much more similar to the motions at sites north of the basin than they are to sites within the basin itself. This suggests that the influence of the basin structure is primarily limited to those sites located in the central basin region, and that the basin generated waves do not “leak” out of the basin in a significant manner.

My primary goals in this study are to model these waveform data to better understand the nature of the basin response in this region and to develop a framework to access how well the data can be modeled as a function of ground shaking frequency. Eventually, this knowledge can be used to help estimate and

quantify the effect of basin response on ground motions for future events in this region (e.g., San Andreas or San Jacinto ruptures).

3D Velocity Structure

The San Bernardino region of southern California is situated on a wedge-shaped sedimentary basin bounded to the north by the San Andreas fault and to the south by the San Jacinto fault (Figure 1). The shape of the bedrock surface underlying the basin sediments has been determined from the analysis of potential field data (Anderson et al., 2000). Figure 3 plots contours of basin depth from the Anderson et al (2000) model. The basin depth is quite shallow along the San Andreas fault and increases towards the southwest, reaching a maximum of about 1800 m just north of the San Jacinto fault. Southwest of this point, the basement surface steps up abruptly and has an average depth of about 300 m in the Fontana basin west of the fault.

In the previous study of the Hector Mine earthquake, Graves and Wald (2004) developed a 3D velocity structure using this basement surface (their Model A). That study used a minimum shear wave velocity of 600 m/s in the basin and the modeling bandwidth was restricted to periods of 2 second and longer. In order to more accurately model the shorter period (T > 1 sec) data in this study, I have reduced this minimum velocity threshold to 250 m/s. This shear wave velocity is consistent with a class D site type, which has an expected V_s^{30} value in the range of 180 m/s to 360 m/s (Wills et al., 2000). Most of the sites in the San Bernardino basin are class CD or D (Wills et al., 2000, Figure 1). Additionally, I have added a gradient in the near surface of the media outside the basin, which lowers the surface shear wave velocity to 700 m/s. This is consistent with a class B site type (Wills et al., 2000). The background velocity structure is given in Table 3.

Figure 4 shows shear wave velocity cross sections through the basin structure taken along profiles A-A' and B-B' (profile locations shown in Figure 3). Profile A-A' crosses near the deepest part of the basin where the sediment thickness is about 1.6 km. Profile B-B' crosses through the north-central portion of the basin where the maximum sediment thickness is only about 800 m. Sediment shear wave velocities range from 250 m/s at the surface to about 1200 m/s in the deep basin. Currently, there is little direct information regarding the velocity structure of the deep basin. The values I use are based on limited P-wave velocity estimates (Hadley and Combs, 1974; Stephenson et al., 2002), as well as the previous modeling work with the Hector Mine data. In this study, the velocity model has been subsequently adjusted using a trial-and-error procedure in an attempt to improve the fit to the ground motion data. Representative velocity profiles for a site outside the basin (**svd**) and a deep basin site (**5329**) are shown in Figure 5. Anelastic attenuation is modeled using $Q_s = 60 \times V_s$ where V_s is given in km/s, and $Q_p = 2 \times Q_s$.

Projected locations of nearby strong motion sites are indicated along each of the cross sections. The character of the ground motions recorded at sites along profile A-A' is noticeably different from the character of motions recorded along profile B-B' (see Figure 2b). For example, the four sites located over the deep basin along profile A-A' (**5341**, **23542**, **5329**, **23780**) have much larger motions and extended shaking durations relative to sites located over the shallower parts of the basin in profile B-B' (**5330**, **23898**, **5337**), as indicated in Figure 2b. The nature of these motions suggests that wave energy is channeled into the deeper sediments as body waves are converted into basin surface waves, thus leading to the amplified motions and longer durations of shaking.

Ground Motion Simulations

I calculate the ground motions using a visco-elastic 3D finite-difference procedure (Graves, 1996) with attenuation modeled using coarse-grain operators (Day and Bradley, 2001; Graves and Day, 2003). The

grid spacing is set at 0.05 km, which coupled with the minimum shear velocity threshold of 250 m/s yields a reliable bandwidth resolution of T > 1 sec within the lowest velocity regions of the simulation model. The model region covers an area of 65 km by 74 km and extends to a depth of 25 km, which requires 962 x 10^6 grid points. The simulations were run on the HPCC Linux Cluster at USC.

The Big Bear Lake earthquake is modeled as a point double-couple source. The mechanism of the event was originally determined using regional waveform data from the Terrascope network and an automated inversion procedure (Zhu and Helmberger, 1996). Using a trial and error procedure, I adjusted the original mechanism slightly in order to improve the waveform fit at the nearby strong motion sites. The moment magnitude of the event is 4.63, the source depth is 7.5 km and the mechanism is primarily strike-slip. Table 1 lists the event information used in the simulation.

As a first step in the modeling procedure I compare the simulated and recorded waveforms at several sites surrounding the basin region. This was done to confirm the accuracy of the source description and to ensure that the wave field propagating into the basin region is modeled properly. Figure 6 compares recorded and simulated three-component ground velocity waveforms for seven sites surrounding the basin region. These sites are plotted with increasing epicentral distance from a minimum of 3.7 km at **bbr** to a maximum of 51.9 km at **rvr**. The data for the N-S component at **bbr** was not usable due to baseline contamination of the original time history. Both data and synthetics have been filtered at T > 3 sec using a fourth-order, zero-phase butterworth operator. All of the data are plotted with respect to absolute time. For most of these sites the waveform and amplitude agreement between the simulated and observed traces is very good, indicating that the source description and background velocity structure are suitable for this bandwidth. The notable exception is station **sbpx**. I suspect the poor fit at **sbpx** is related to geologic complexity that is not included in the simulation model in the vicinity of this location.

Figure 7 compares profiles of recorded and simulated horizontal ground velocities for a number of the sites located inside the basin region. Both sets of time histories have been rotated into radial and tangential components relative to the epicenter, and have been band pass filtered at T > 3 sec. The order of the sites plotted in Figure 7 is the same as in Figure 2, although I have not included the CSMIP sites in Figure 7 because the filter corner is beyond the useable bandwidth of these data.

For most of the sites in Figure 7, the simulated motions match the amplitude and waveform of the recorded motions reasonably well. As noted earlier, the recorded motions at the basin sites exhibit more waveform complexity and longer durations relative to sites north and south of the basin. The simulation reproduces nicely the motions at sites in the northern basin (**5162**, **5337**, **5373**) and in the south-central basin (**0129**, **5328**, **5431**), both in terms of peak amplitude and duration. The amplitudes of the radial motions are matched quite well, whereas the simulation tends to overpredict the amplitudes of the tangential motions at the deep basin sites. The longest observed durations are for the group of sites in the mid-central portion of the basin (**5339**, **clt**, **5329**). Although the simulation matches the peak motions at these sites, it generally underpredicts the total durations. This suggests that the basin structure may need some refinement in the mid-central basin region. In particular, expanding the deep basin trough toward the northeast would increase the potential for trapping surface wave energy in the vicinity of these sites.

Figure 8 plots profiles of the simulated ground velocities filtered at T > 1 sec. For this pass band, I also include the response simulated for the CSMIP sites. The simulated motions reproduce many of the characteristics seen in the observed motions, as shown in Figure 2. These characteristics include relatively simple waveforms north of the basin, increased amplitudes and extended durations within the basin, and reduction of amplitudes and decreased waveform complexity south of the basin. Despite this general agreement, the simulated motions tend to underpredict the overall durations of the observed motions. This is true both for sites inside (e.g., **5329**) as well as outside (e.g., **5331**) the basin. This

suggests that the 3D model does not contain enough structural complexity at the shorter length scales to adequately represent the real structure.

In order to more closely examine the fitness of the simulation model as a function of ground motion period, I compare the recorded and simulated three component time histories for 16 sites in pass bands of T > 3 sec, T > 2 sec, and T > 1 sec (Figure 9). Again, at the longer periods (T > 3 sec), the match between the simulated and observed motions is good. Going to a somewhat shorter period band (T > 2 sec), it is apparent that the fit begins to worsen. This is true not only at the basin sites, but also at the non-basin sites, e.g., **svd**. Although the first few cycles of motion tend to be matched with reasonable accuracy, the fit deteriorates with time into the record. This same trend continues to the shortest period band (T > 1 sec). In addition, the simulation tends to underpredict the peak amplitudes and the shaking durations more severely at the shorter periods.

Figures 10, 11 and 12 compare, respectively, the peak amplitude, duration (5 to 75% of total energy) and cross-correlation of the observed and simulated ground velocities for 22 sites in pass bands of T > 3 sec, T > 2 sec, and T > 1 sec. In these figures, the stations are plotted in order of generally increasing epicentral distance with sites located in the central basin region indicated by the gray shading. The results are displayed separately for the tangential, radial and vertical components.

In all three pass bands, the observed peak amplitudes show a similar pattern of elevated levels for the basin sites (Figure 10). This pattern is strongest on the horizontal components, and less prominent on the vertical component. This amplification pattern is matched well by the simulations. In addition, the simulation generally reproduces the absolute level of the tangential motions, and tends to underpredict the level of the radial and vertical motions. It should be noted that the peak amplitudes are measured for the entire time history, independent of phasing; thus the location of the peak motion on the simulated time history may be different than that for the observed time history.

The observed duration measures plotted in Figure 11 show little systematic variation, either as a function of pass band, component or site type (i.e., basin or non-basin). However, there is a general increase of duration as a function of epicentral distance. Both the absolute level and trend of the observed durations are matched well by the simulations. It is somewhat surprising that the duration measures plotted in Figure 11 exhibit little difference for basin and non-basin sites, especially when the visual appearance of the time histories in Figures 2 and 7 suggest that the basin sites have noticeably longer durations than the non-basin sites. I suspect that this occurs because the coda at the non-basin sites, while of low amplitude, is still significant enough to contribute to the duration measure. I explored several variations in the cutoff percentages for the duration measures (e.g., 5 to 50%, 5 to 95%, 25 to 75%), but the general pattern of the results remained unchanged.

The cross-correlation measures in Figure 12 show a strong systematic pattern of decreasing correlation with decreasing minimum period. The correlation coefficients average around 0.8 for the passband T > 3 sec, 0.4-0.5 for the passband T > 2 sec, and 0.3 for the passband T > 1 sec. Although there is significant scatter in these measurements, there appears to be no strong systematic trend as a function of site type or component. Since the propagation distances are relatively short, I have allowed a time shift within the range of +/- 1 sec in determining the maximum of the cross correlation. The lower panels of Figure 12 indicate the time shift of the correlation maximum for each site and each period. In general, there is little systematic trend in the pattern of the time shifts, either as a function of site location or period band. I suspect that the time shifts are indicative of small misfits to the variability of the true velocity structure that are not included in the current model.

Discussion and Conclusions

The results of the previous section indicate that waveform modeling in the San Bernardino basin region can reproduce the amplitudes, waveforms and durations of recorded motions quite well at periods of 3 seconds and longer. This period threshold is similar to that found by Komatitsch et al. (2004) in their modeling of small event waveforms in the Los Angeles basin region. At shorter periods, the modeling is still able to capture the main trends in peak amplitude (Figure 10) and overall duration (Figure 11), but the reproduction of waveform details is much less well resolved (Figure 12). These results suggest that the general nature of the 3D velocity structure is well resolved; however, the details of the structure, which are important for the shorter period energy, are less well resolved.

Traditionally, there have been two main issues that involved in pushing the modeling resolution to shorter periods. The first is purely a computational issue. That is, accurate numerical modeling of shorter period energy with grid-based techniques requires the use of finer grid sampling. This, in turn, requires more computational resources. Fortunately, continued advancement in computational infrastructure (e.g., 64 bit architecture, widespread accessibility to PC/Linux clusters, etc.) along with refinements of the modeling algorithms (e.g., parallelized finite/spectral-element and finite-difference codes, variable grid finite-difference methods, etc.) have made the simulation of realistic models much more feasible. The present study is an example of this where the ground motions have been computed down to 1 second period within media having relatively low seismic velocities (250 m/s).

The second and arguably more important issue is related to our limited knowledge of earth structure and earthquake source processes. The current study uses a minimum shear wave velocity within the basin sediments of 250 m/s. As noted earlier, there is little direct information about the shear wave velocities in the basin sediments. The value of 250 m/s is consistent with a NEHRP class D or CD site type, which is typical of the sites within the San Bernardino basin. It is likely that the model I have constructed for the

current simulation does not contain sufficient variability in the basin velocity structure, particularly in the near surface, to adequately generate the waveform complexity seen in the recorded motions at periods around 1 sec. Although the grid spacing used in the FD model is 50 m, the lateral variability of the velocity layers within the current basin model is much smoother (on the order of 500 m or larger). One obvious modification to the current model would be to introduce small scale lateral fluctuations in the velocity structure of the shallow basin (e.g., Frankel and Clayton, 1984). Unfortunately, without specific information to guide this process, it is unlikely that the deterministic fit to the observed waveforms would be improved. Another alternative is to use the current model as the starting point for a full 3D waveform inversion (e.g., Chen et al, 2006; Liu and Tromp, 2006). This is the topic for future study.

Furthermore, as the modeling is pushed toward shorter periods, the details of the velocity structure *outside* of the basin region begin to become important, as well. This is illustrated in Figure 13, which displays ground velocity time histories recorded at three TerraScope sites outside of the San Bernardino basin. Motions for two events are shown: thick traces are for the M_w 4.63 Big Bear Lake event and thin traces are for a M_w 3.2 aftershock which occurred very close to the mainshock. The motions for the smaller event have been scaled by a factor of 250 to account for the difference in moment. Both sets of motions have been filtered at T > 1 sec. The use of small events such as these for basin validation studies is attractive because the source process can usually be regarded as "simple" in the period range where the modeling is targeted (typically T > 1 sec).

The similarity in the amplitudes and waveforms for the two events is remarkable. Since these events differ by over two units in magnitude, this suggests that the complexities seen in the waveforms are due to path and site effects, as opposed to source effects. In the absence of path and site complexities, we would expect the motions at these stations to be characterized by simple pulses of motion related to the direct P and S waves. However, the motions exhibit significant arrivals following the main pulses and lasting in duration for 5 to 10 seconds. Granted, the complexity of these motions is not nearly as strong as seen at

the basin sites where the large amplitude later arrivals can last in duration for 50 seconds or more. Nonetheless, the complexity at these non-basin sites is indicative of the characteristics of the wave field as it propagates into the basin region. I suspect that the response at these stations may be effected by topography, local site conditions (e.g., **svd** is in a zone of very complex geology adjacent to the San Andreas fault), or small basin type structures (e.g., **bbr** is in a small valley containing Big Bear Lake). In my modeling, I have not attempted to match all of the details of the response at these non basin sites, but rather to capture the main characteristics of the motion as it propagates into the basin region. Ultimately, a more complete realization of the motions at all of the sites (basin *and* non-basin) will require very detailed knowledge of the subsurface geology and seismic velocity structure.

Acknowledgements

This research was supported by funding from the USGS External Grants Program (02HQ0096 and 03HQ0085) and the Southern California Earthquake Center (SCEC). The simulations were run at the University of Southern California Center for High Performance Computing and Communications (http://www.usc.edu/hpcc). Figures were composed using GMT software (Wessel and Smith, 1998).

References

Anderson, M. L., C. W. Roberts, and R. C. Jachens (2000). Principal facts for gravity stations in the vicinity of San Bernardino, southern California, *U.S. Geol. Surv. Open-File Rept. 00-193*, 32 pp.

Boore, D. M., C. D. Stephens, and W. B. Joyner (2002). Comments on baseline correction of digital strong motion data: examples from the 1999 Hector Mine, California, earthquake, *Bull. Seism. Soc. Am.*, **92**, 1543–1560.

Chen, P., L. Zhao and T. H. Jordan (2006). Full 3D tomography for crustal structure of the Los Angeles region, *Bull. Seism. Soc. Am.*, in press.

Day, S. M., and C. R. Bradley (2001). Memory efficient simulation of anelastic wave propagation, *Bull. Seism. Soc. Am.* **91**, 520–531.

Frankel, A. (1994). Dense array recordings in the San Bernardino valley of Landers-Big Bear aftershocks: basin surface waves, Moho reflections, and three-dimensional simulations, *Bull. Seism. Soc. Am.*, **84**, 613–624.

Frankel, A. and R. W. Clayton (1984). A finite-difference simulation of wave propagation in two-dimensional random media, *Bull. Seism. Soc. Am.* **74**, 2167-2186.

Graves, R. W. (1996). Simulating seismic wave propagation in 3D elastic media using staggered grid finite differences, *Bull. Seism. Soc. Am.*, **86**, 1091–1106.

Graves, R. W. and Steven M. Day (2003). Stability and accuracy analysis of coarse-grain viscoelastic simulations, *Bull. Seism. Soc. Am.*, **93**, 283-300.

Graves, R. W. and David J. Wald (2004). Observed and simulated ground motions in the San Bernardino basin region for the Hector Mine, California, earthquake, *Bull. Seism. Soc. Am.*, **94**, 131–146.

Hadley, D. and J. Combs (1974). Microearthquake distribution and mechanisms of faulting in the Fontana-San Bernardino area of southern California, *Bull. Seism. Soc. Am.*, **64**, 1477-1499.

Komatitsch, D., Qinya Liu, Jeroen Tromp, Peter Suess, Christiane Stidham, and John H. Shaw (2004). Simulations of ground motion in the Los Angeles basin based upon the spectral-element method, *Bull. Seism. Soc. Am.*, **94**, 187-206.

Liu, Q. and J. Tromp (2006). Finite-frequency kernels based upon adjoint methods, *Bull. Seism. Soc. Am.*, in press.

Stephenson, W. J., J. K. Odum, R. A. Williams and M. L. Anderson (2002). Delineation of faulting and basin geometry along a seismic reflection transect in urbanized San Bernardino valley, California, *Bull. Seism. Soc. Am.*, **92**, 2504-2520.

Wessel, P., and W. H. F. Smith (1998). New, improved version of Generic Mapping Tools released, *EOS Trans. Amer. Geophys. U.*, **79** (47), pp. 579.

Wills, C. J., M. Petersen, W. A. Bryant, M. Reichle, G. J. Saucedo, S. Tan, G. Taylor, and J. Treiman (2000). A Site-Conditions Map for California Based on Geology and Shear-Wave Velocity, *Bull. Seism. Soc. Am.*, **90**, S187-S208.

Zhu, L. and D. V. Helmberger (1996). Advancement in source estimation techniques using broadband regional seismograms, *Bull. Seism. Soc. Am.*, **86**, 1634-1641.

Table 1: Source parameters.

Date	02/10/01
Origin Time	21:05:05.34
Latitude	34.2913
Longitude	-116.9403
Moment	1×10^{23} dyne-cm
Depth	7.5 km
Strike	208°
Dip	77°
Rake	10°

Table 2: Station information.

Station Code	Dist. (km)	Azimuth	Longitude	Latitude	Site Type	Operator	Bandwidth (sec)
bbr	3.7	151	-116.9207	34.2623	D	CIT/USGS	0.04 – 10
svd	25.2	215	-117.0982	34.1065	BC	CIT/USGS	0.04 – 10
5076	25.5	202	-117.0448	34.0793	C	NSMP	0.04 – 10
sbpx	27.9	256	-117.2348	34.2322	BC	CIT/USGS	0.04 – 10
5162	29.8	213	-117.1170	34.0670	D	NSMP	0.04 – 10
5336	30.3	238	-117.2187	34.1449	C	NSMP	0.04 – 10
5161	30.5	235	-117.2133	34.1360	CD	NSMP	0.04 – 10
5331	31.7	244	-117.2507	34.1665	BC	NSMP	0.04 – 10
23897	33.7	239	-117.2530	34.1340	D	CSMIP	0.025 – 3
5327	35.0	246	-117.2890	34.1652	D	NSMP	0.04 – 10
5337	36.6	243	-117.2939	34.1400	D	NSMP	0.04 – 10
5373	37.0	240	-117.2870	34.1228	D	NSMP	0.04 – 10
23780	38.4	236	-117.2860	34.0970	D	CSMIP	0.025 – 3
5339	39.1	235	-117.2902	34.0917	D	NSMP	0.04 – 10
23898	39.2	244	-117.3220	34.1350	D	CSMIP	0.025 – 3
5329	39.5	231	-117.2754	34.0691	D	NSMP	0.04 – 10
lug	40.0	282	-117.3658	34.3661	CD	CIT/USGS	0.04 – 10
0129	40.1	228	-117.2642	34.0503	D	NSMP	0.04 – 10
23542	41.0	232	-117.2920	34.0650	D	CSMIP	0.025 – 3
5328	41.2	229	-117.2770	34.0469	D	NSMP	0.04 – 10
bbs	41.3	185	-116.9809	33.9214	C	CIT/USGS	0.04 – 10
5341	42.4	232	-117.3048	34.0580	CD	NSMP	0.04 – 10
5330	43.0	241	-117.3486	34.1030	CD	NSMP	0.04 – 10
5265	43.4	262	-117.4076	34.2350	CD	NSMP	0.04 – 10
23788	44.8	237	-117.3500	34.0740	CD	CSMIP	0.025 – 3
fon	50.6	245	-117.4388	34.0996	CD	CIT/USGS	0.04 – 10
rvr	51.9	230	-117.3755	33.9935	CD	CIT/USGS	0.04 – 10

Table 3: Background velocity structure.

Vp (km/s)	Vs (km/s)	Density (g/cc)	Depth (km)
1.9	0.7	2.2	0.025
2.4	1.2	2.3	0.125
3.3	1.7	2.4	0.5
4.6	2.4	2.5	2.6
6.0	3.45	2.6	6.2
6.3	3.6	2.8	28.0
7.95	4.5	3.0	-

Figure Captions

Figure 1: Map of the San Bernardino region of Southern California showing location of the 2001 Big Bear Lake earthquake and strong motion recording sites. Dark and light gray shading indicate surface exposure of site class types CD and D, respectively (Wills et al., 2000). The San Bernardino basin lies in the wedge shaped region between the San Andreas and San Jacinto faults, and is covered by a dense cluster of strong motion recording sites.

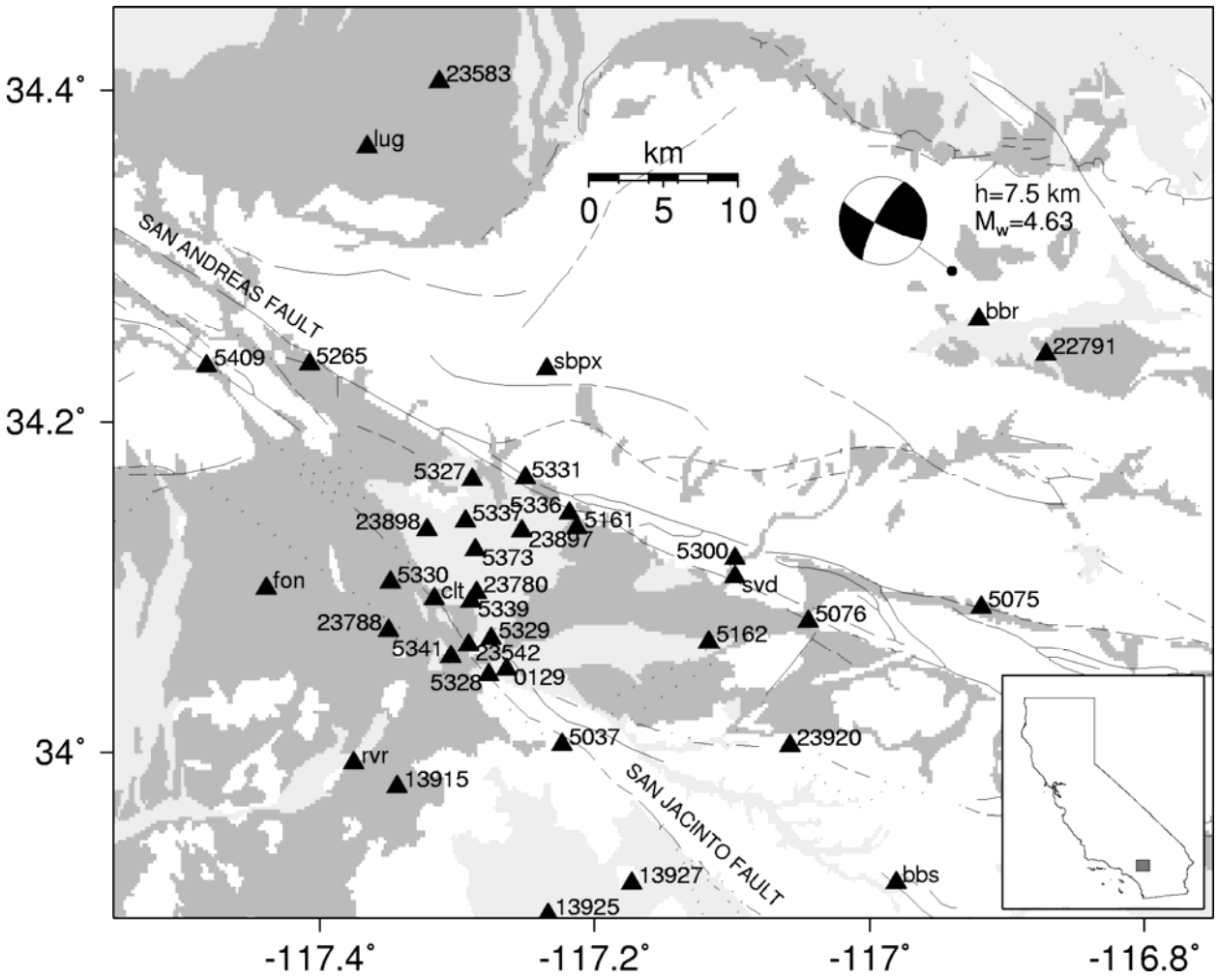
34.4˚
34.2˚
34˚
-117.4˚
-117.2˚
-117˚
-116.8˚
km
0 5 10
h=7.5 km
M_w=4.63
SAN ANDREAS FAULT
SAN JACINTO FAULT
23583
lug
bbr
22791
5409
5265
sbpx
5327
5331
5336
5337
5161
23898
23897
5373
5300
fon
5330
clt
23780
svd
5339
5075
5076
23788
5329
5162
5341
23542
5328
0129
5037
23920
rvr
13915
13927
bbs
13925

Figure 1.

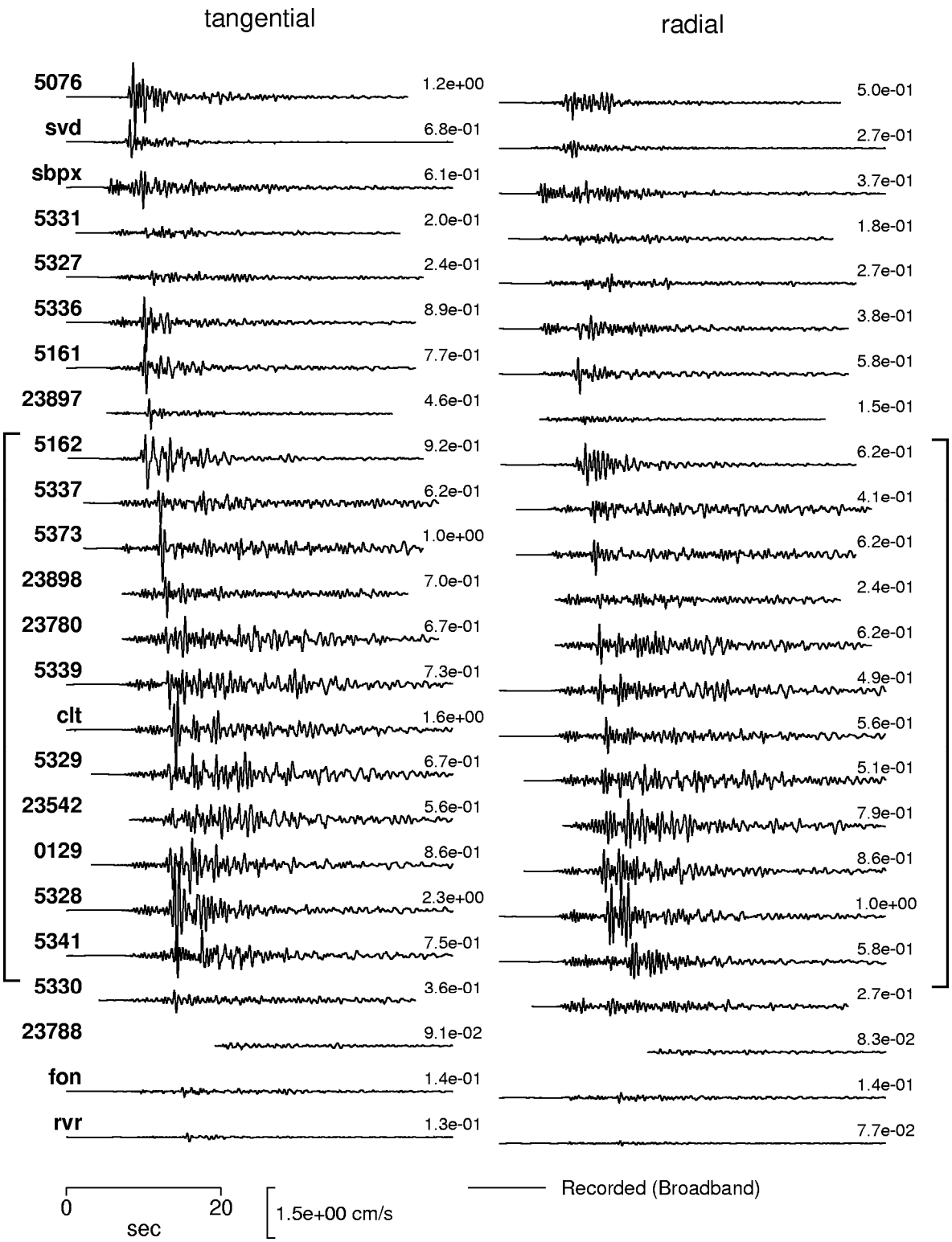
tangential
radial
5076
svd
sbpx
5331
5327
5336
5161
23897
5162
5337
5373
23898
23780
5339
clt
5329
23542
0129
5328
5341
5330
23788
fon
rvr
1.2e+00
6.8e-01
6.1e-01
2.0e-01
2.4e-01
8.9e-01
7.7e-01
4.6e-01
9.2e-01
6.2e-01
1.0e+00
7.0e-01
6.7e-01
7.3e-01
1.6e+00
6.7e-01
5.6e-01
8.6e-01
2.3e+00
7.5e-01
3.6e-01
9.1e-02
1.4e-01
1.3e-01
5.0e-01
2.7e-01
3.7e-01
1.8e-01
2.7e-01
3.8e-01
5.8e-01
1.5e-01
6.2e-01
4.1e-01
6.2e-01
2.4e-01
6.2e-01
4.9e-01
5.6e-01
5.1e-01
7.9e-01
8.6e-01
1.0e+00
5.8e-01
2.7e-01
8.3e-02
1.4e-01
7.7e-02
0
20
sec
1.5e+00 cm/s
Recorded (Broadband)

Figure 2a.

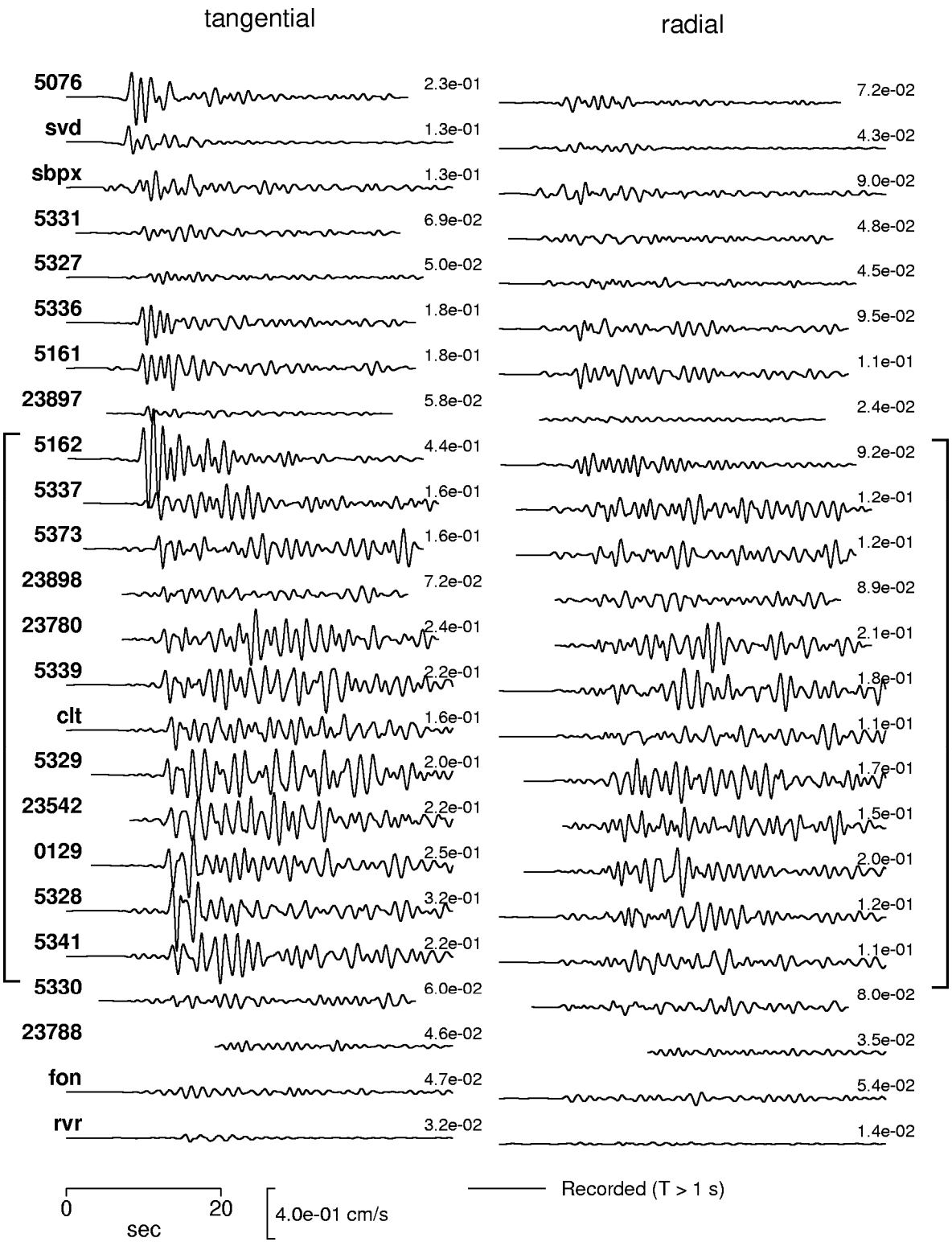
tangential
radial
5076
svd
sbpx
5331
5327
5336
5161
23897
5162
5337
5373
23898
23780
5339
clt
5329
23542
0129
5328
5341
5330
23788
fon
rvr
2.3e-01
1.3e-01
1.3e-01
6.9e-02
5.0e-02
1.8e-01
1.8e-01
5.8e-02
4.4e-01
1.6e-01
1.6e-01
7.2e-02
2.4e-01
2.2e-01
1.6e-01
2.0e-01
2.2e-01
2.5e-01
3.2e-01
2.2e-01
6.0e-02
4.6e-02
4.7e-02
3.2e-02
7.2e-02
4.3e-02
9.0e-02
4.8e-02
4.5e-02
9.5e-02
1.1e-01
2.4e-02
9.2e-02
1.2e-01
1.2e-01
8.9e-02
2.1e-01
1.8e-01
1.1e-01
1.7e-01
1.5e-01
2.0e-01
1.2e-01
1.1e-01
8.0e-02
3.5e-02
5.4e-02
1.4e-02
0
20
sec
4.0e-01 cm/s
Recorded (T > 1 s)

Figure 2b.

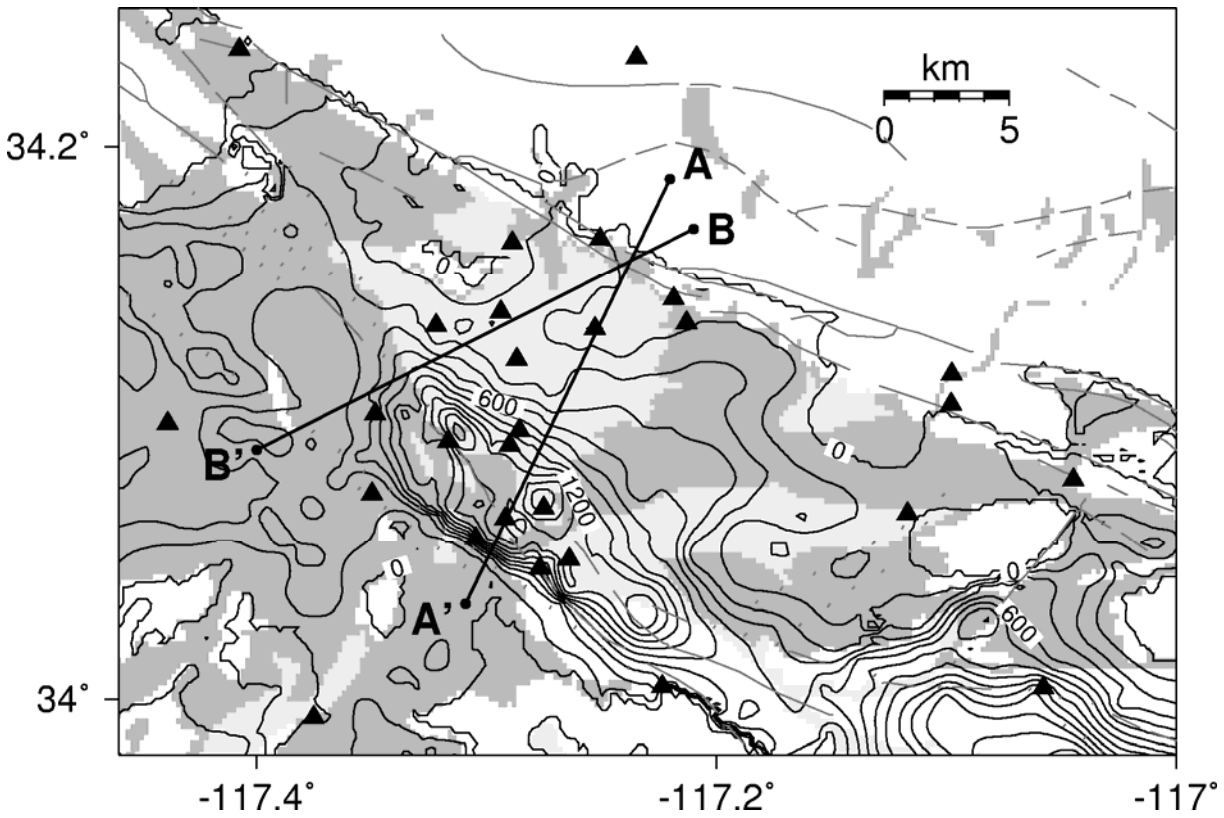

Figure 3.

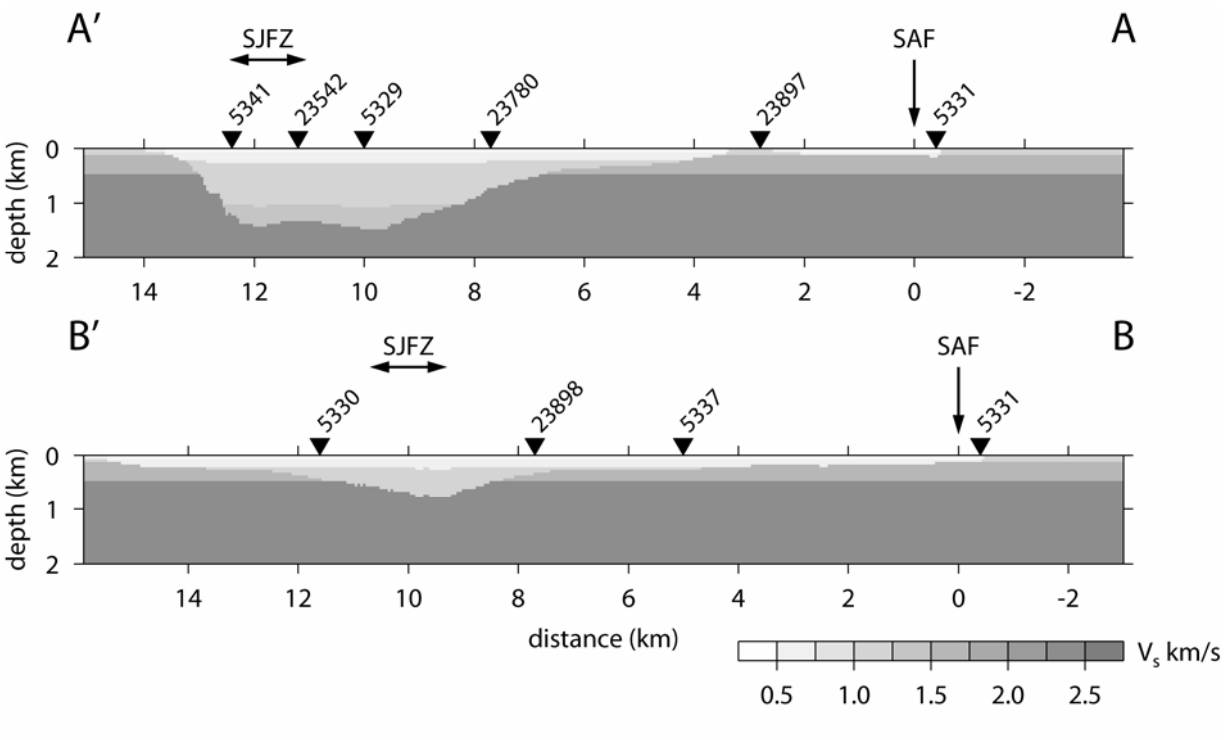
A′
SJFZ
SAF
A
5341
23542
5329
23780
23897
5331
depth (km)
0
1
2
14
12
10
8
6
4
2
0
-2
B′
SJFZ
SAF
B
5330
23898
5337
5331
depth (km)
0
1
2
14
12
10
8
6
4
2
0
-2
distance (km)
V_s km/s
0.5
1.0
1.5
2.0
2.5

Figure 4.

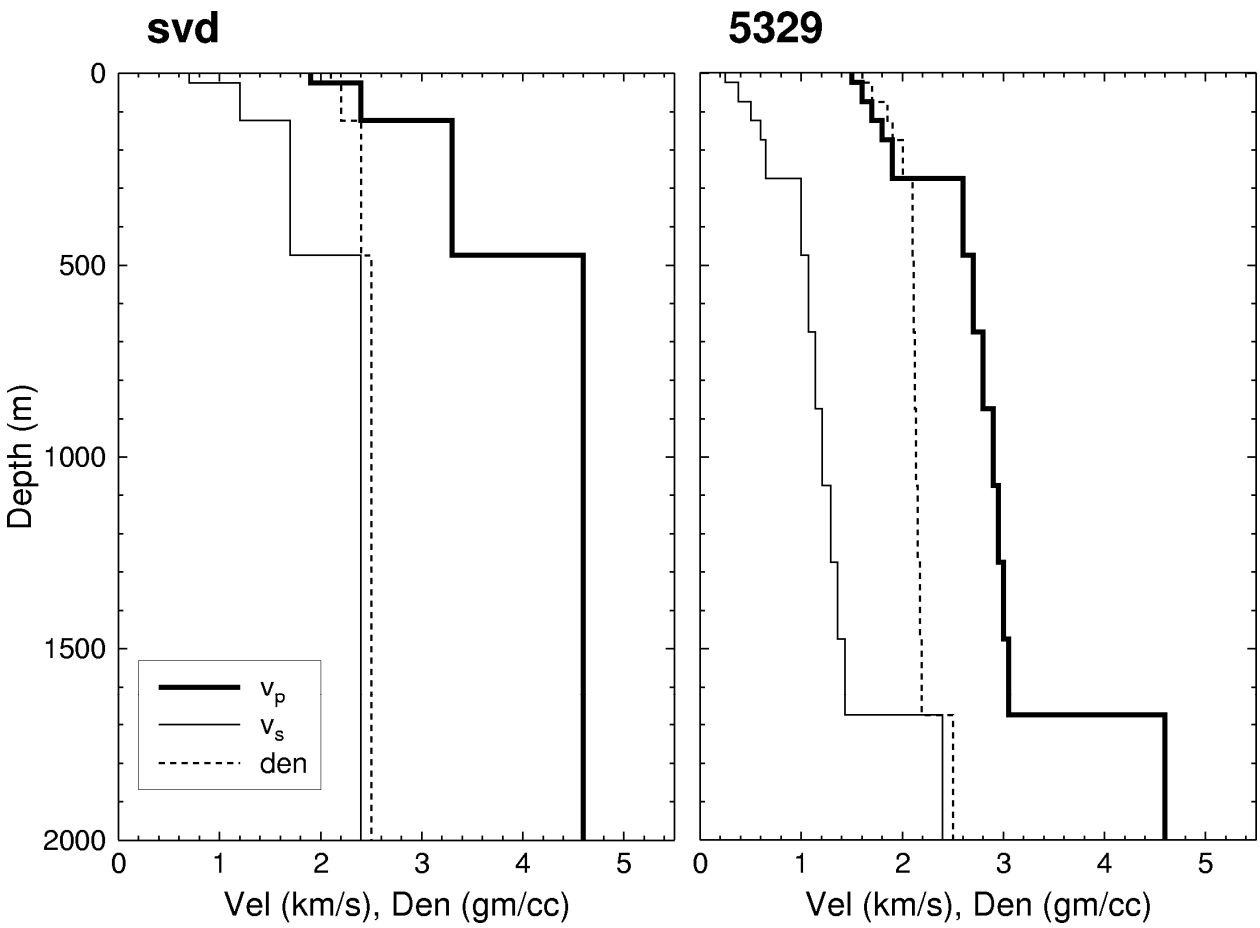
svd
5329
Depth (m)
0
500
1000
1500
2000
0
1
2
3
4
5
Vel (km/s), Den (gm/cc)
Vel (km/s), Den (gm/cc)
v_p
v_s
den

Figure 5.

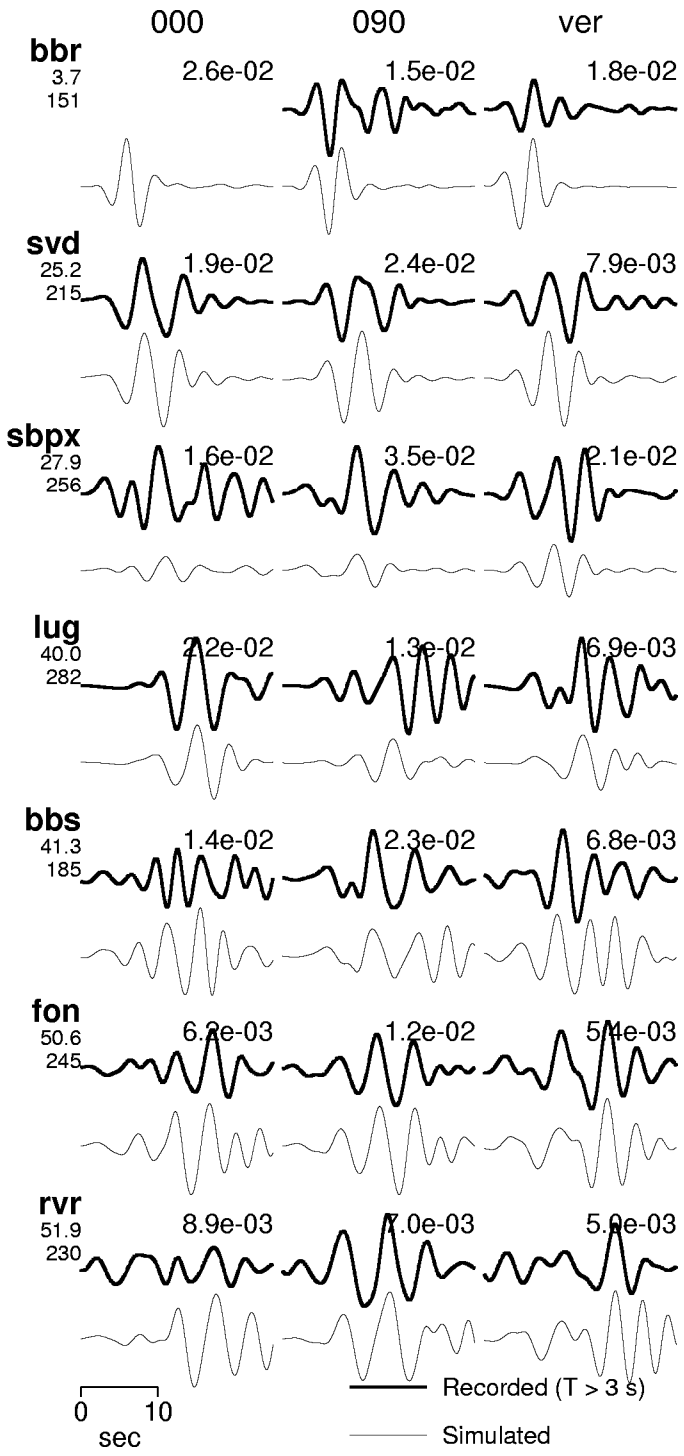
000
090
ver
bbr
3.7
151
2.6e-02
1.5e-02
1.8e-02
svd
25.2
215
1.9e-02
2.4e-02
7.9e-03
sbpx
27.9
256
1.6e-02
3.5e-02
2.1e-02
lug
40.0
282
2.2e-02
1.3e-02
6.9e-03
bbs
41.3
185
1.4e-02
2.3e-02
6.8e-03
fon
50.6
245
6.2e-03
1.2e-02
5.4e-03
rvr
51.9
230
8.9e-03
7.0e-03
5.0e-03
0
10
sec
Recorded (T > 3 s)
Simulated

Figure 6.

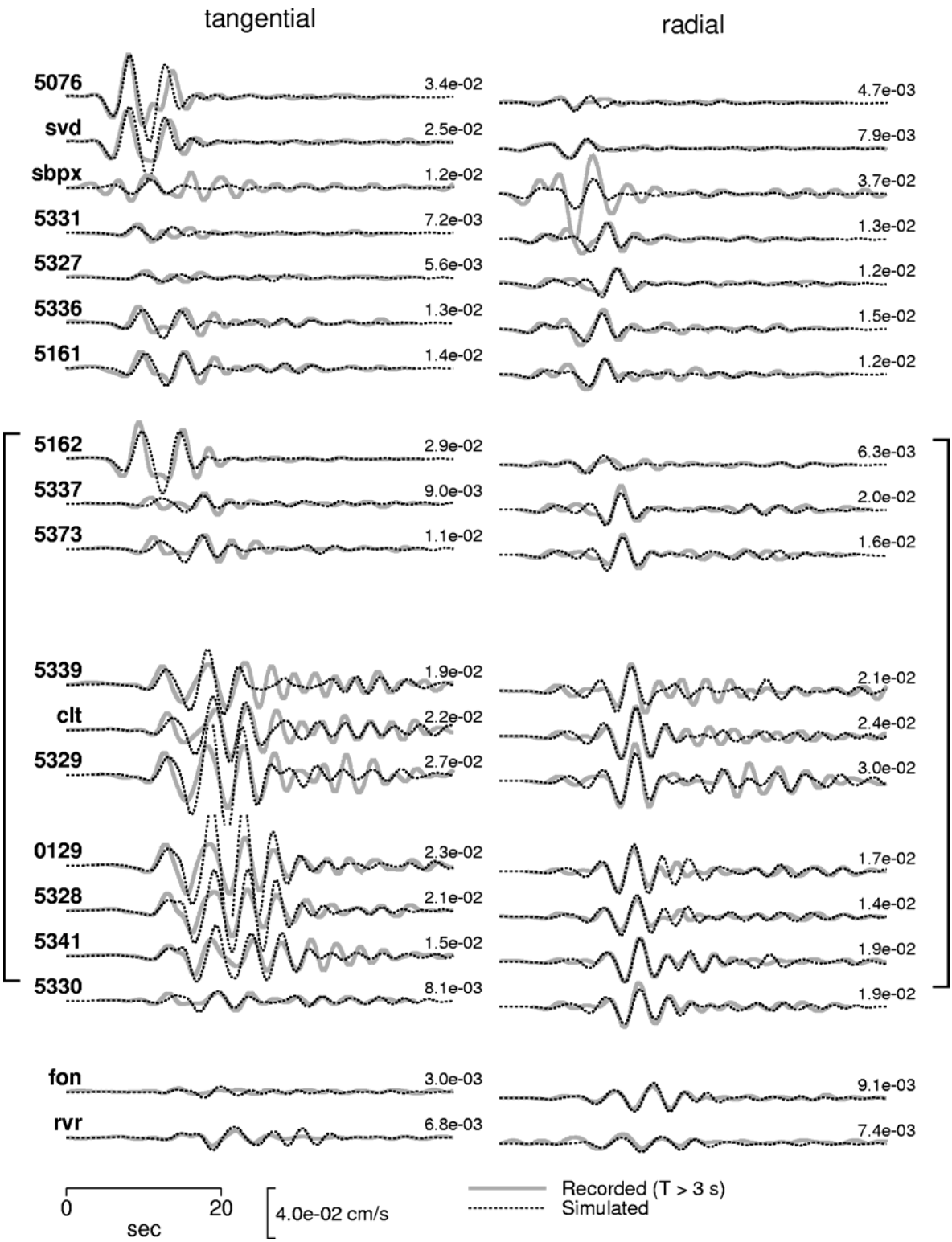
tangential
radial
5076
3.4e-02
4.7e-03
svd
2.5e-02
7.9e-03
sbpx
1.2e-02
3.7e-02
5331
7.2e-03
1.3e-02
5327
5.6e-03
1.2e-02
5336
1.3e-02
1.5e-02
5161
1.4e-02
1.2e-02
5162
2.9e-02
6.3e-03
5337
9.0e-03
2.0e-02
5373
1.1e-02
1.6e-02
5339
1.9e-02
2.1e-02
clt
2.2e-02
2.4e-02
5329
2.7e-02
3.0e-02
0129
2.3e-02
1.7e-02
5328
2.1e-02
1.4e-02
5341
1.5e-02
1.9e-02
5330
8.1e-03
1.9e-02
fon
3.0e-03
9.1e-03
rvr
6.8e-03
7.4e-03
0
20
sec
4.0e-02 cm/s
Recorded (T > 3 s)
Simulated

Figure 7.

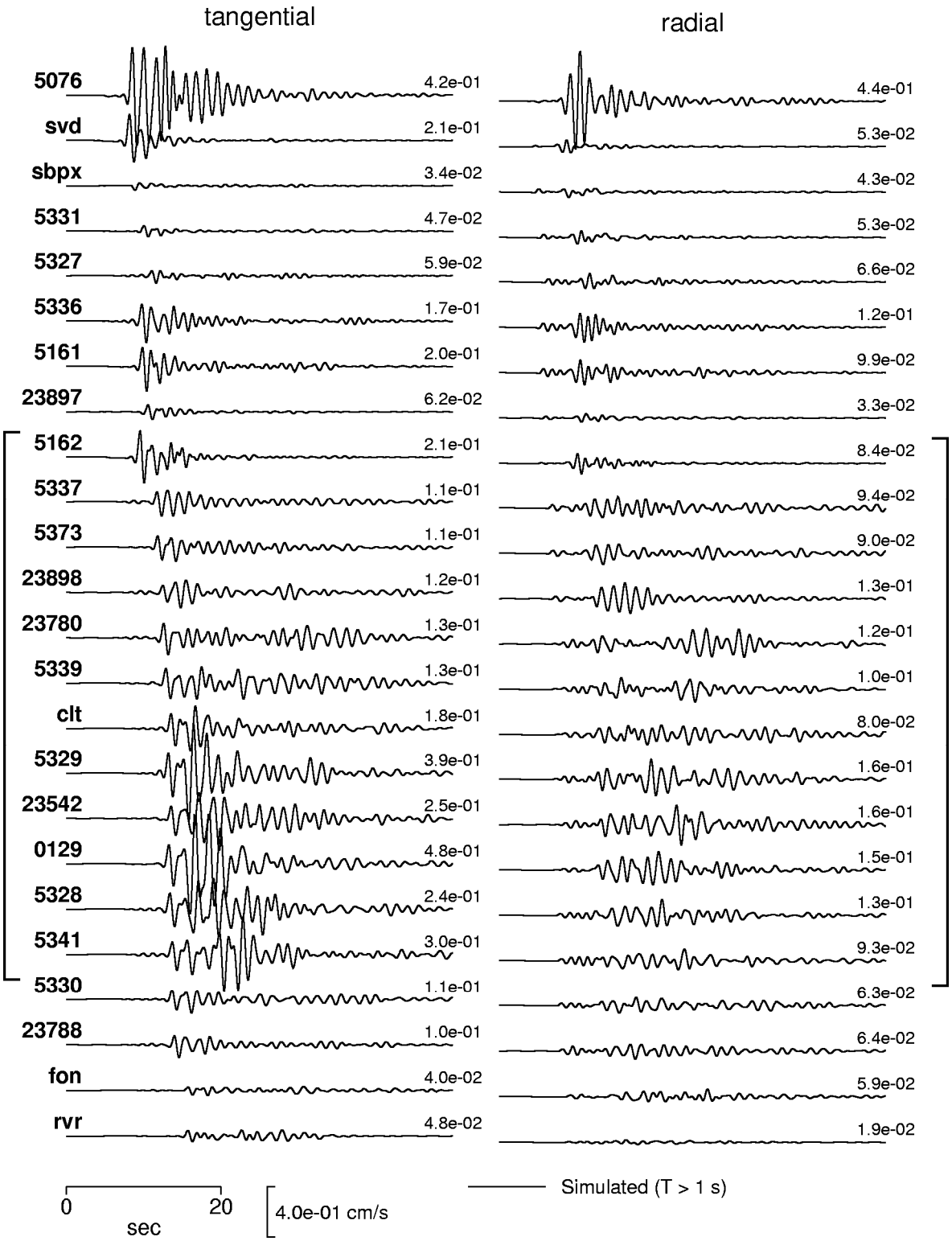
tangential
radial
5076
svd
sbpx
5331
5327
5336
5161
23897
5162
5337
5373
23898
23780
5339
clt
5329
23542
0129
5328
5341
5330
23788
fon
rvr
4.2e-01
2.1e-01
3.4e-02
4.7e-02
5.9e-02
1.7e-01
2.0e-01
6.2e-02
2.1e-01
1.1e-01
1.1e-01
1.2e-01
1.3e-01
1.3e-01
1.8e-01
3.9e-01
2.5e-01
4.8e-01
2.4e-01
3.0e-01
1.1e-01
1.0e-01
4.0e-02
4.8e-02
4.4e-01
5.3e-02
4.3e-02
5.3e-02
6.6e-02
1.2e-01
9.9e-02
3.3e-02
8.4e-02
9.4e-02
9.0e-02
1.3e-01
1.2e-01
1.0e-01
8.0e-02
1.6e-01
1.6e-01
1.5e-01
1.3e-01
9.3e-02
6.3e-02
6.4e-02
5.9e-02
1.9e-02
0
20
sec
4.0e-01 cm/s
Simulated (T > 1 s)

Figure 8.

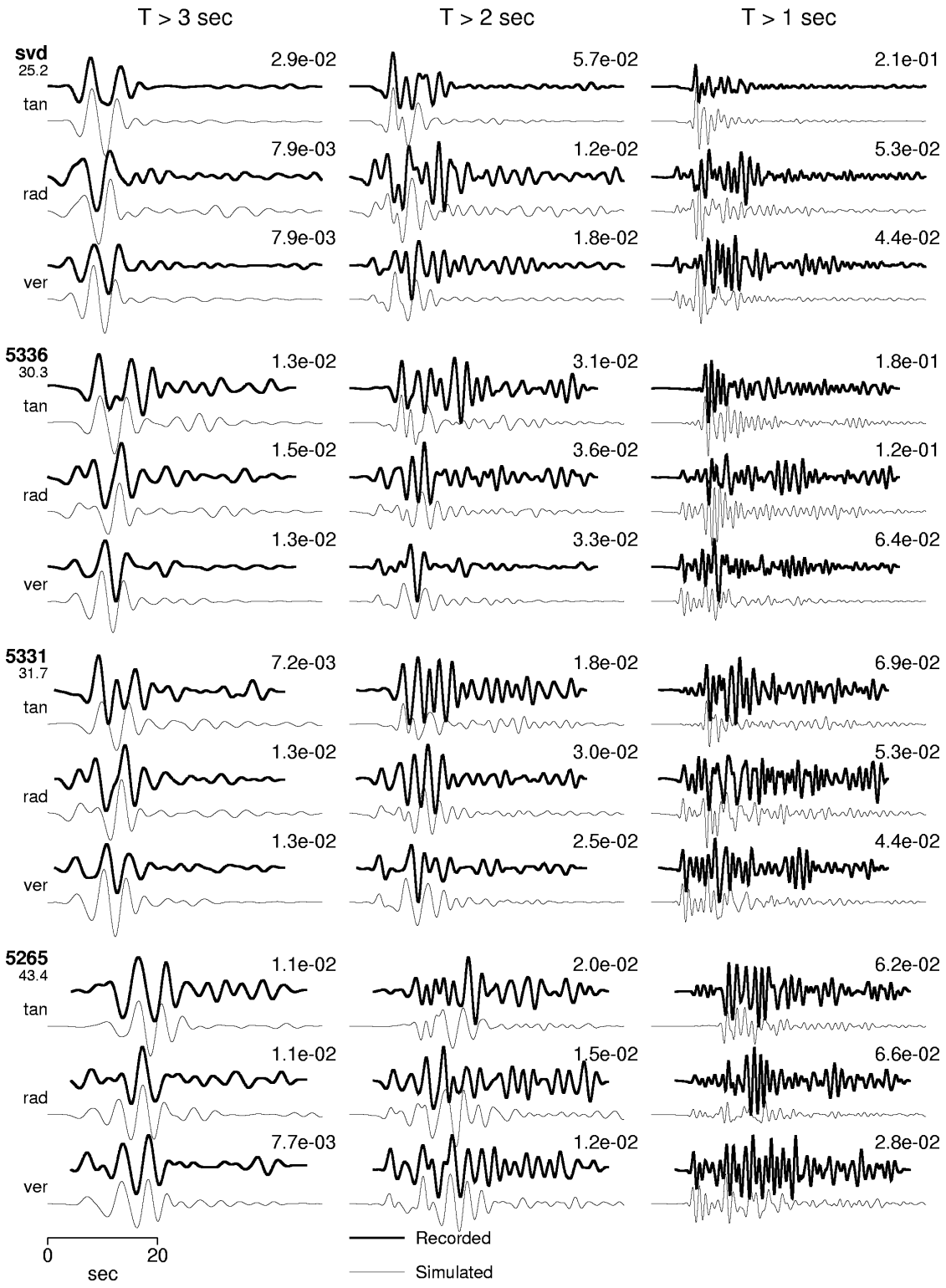
T > 3 sec
T > 2 sec
T > 1 sec
svd
25.2
tan
rad
ver
2.9e-02
7.9e-03
7.9e-03
5.7e-02
1.2e-02
1.8e-02
2.1e-01
5.3e-02
4.4e-02
5336
30.3
1.3e-02
1.5e-02
1.3e-02
3.1e-02
3.6e-02
3.3e-02
1.8e-01
1.2e-01
6.4e-02
5331
31.7
7.2e-03
1.3e-02
1.3e-02
1.8e-02
3.0e-02
2.5e-02
6.9e-02
5.3e-02
4.4e-02
5265
43.4
1.1e-02
1.1e-02
7.7e-03
2.0e-02
1.5e-02
1.2e-02
6.2e-02
6.6e-02
2.8e-02
0
20
sec
Recorded
Simulated

Figure 9a.

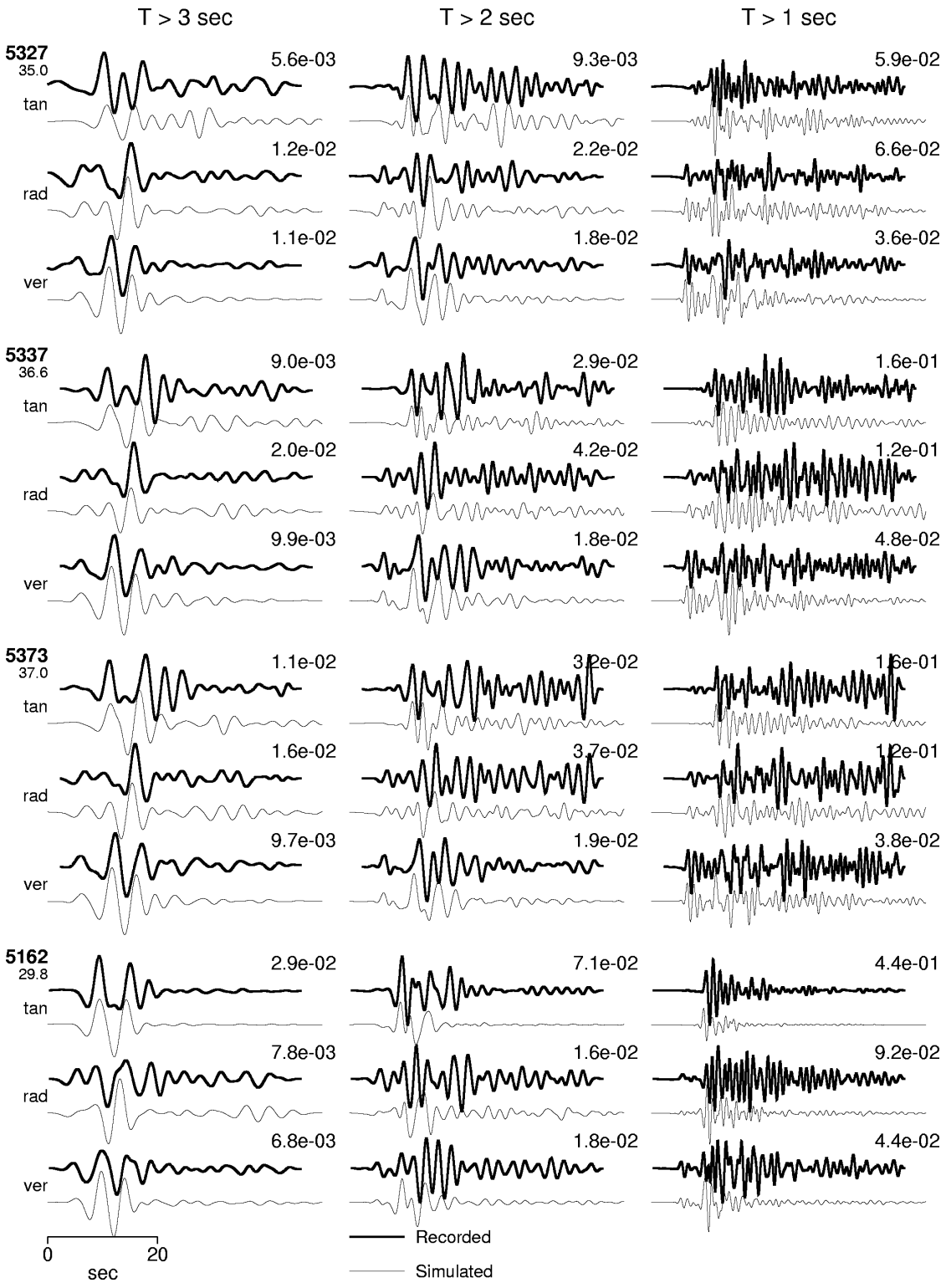
T > 3 sec
T > 2 sec
T > 1 sec
5327
35.0
tan
rad
ver
5.6e-03
1.2e-02
1.1e-02
9.3e-03
2.2e-02
1.8e-02
5.9e-02
6.6e-02
3.6e-02
5337
36.6
9.0e-03
2.0e-02
9.9e-03
2.9e-02
4.2e-02
1.8e-02
1.6e-01
1.2e-01
4.8e-02
5373
37.0
1.1e-02
1.6e-02
9.7e-03
3.2e-02
3.7e-02
1.9e-02
1.6e-01
1.2e-01
3.8e-02
5162
29.8
2.9e-02
7.8e-03
6.8e-03
7.1e-02
1.6e-02
1.8e-02
4.4e-01
9.2e-02
4.4e-02
0
20
sec
Recorded
Simulated

Figure 9b.

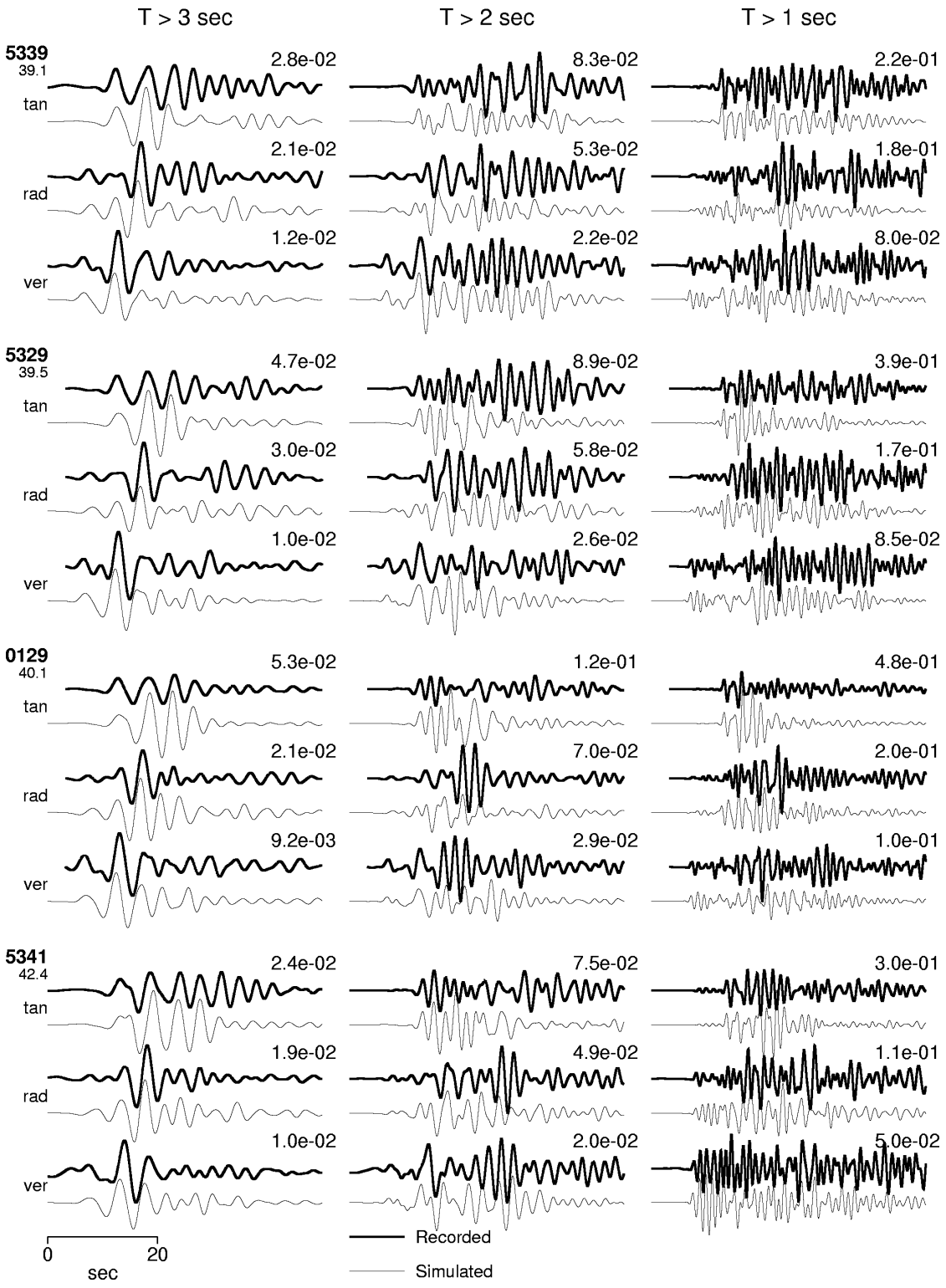
T > 3 sec
T > 2 sec
T > 1 sec
5339
39.1
tan
rad
ver
2.8e-02
2.1e-02
1.2e-02
8.3e-02
5.3e-02
2.2e-02
2.2e-01
1.8e-01
8.0e-02
5329
39.5
4.7e-02
3.0e-02
1.0e-02
8.9e-02
5.8e-02
2.6e-02
3.9e-01
1.7e-01
8.5e-02
0129
40.1
5.3e-02
2.1e-02
9.2e-03
1.2e-01
7.0e-02
2.9e-02
4.8e-01
2.0e-01
1.0e-01
5341
42.4
2.4e-02
1.9e-02
1.0e-02
7.5e-02
4.9e-02
2.0e-02
3.0e-01
1.1e-01
5.0e-02
0
20
sec
Recorded
Simulated

Figure 9c.

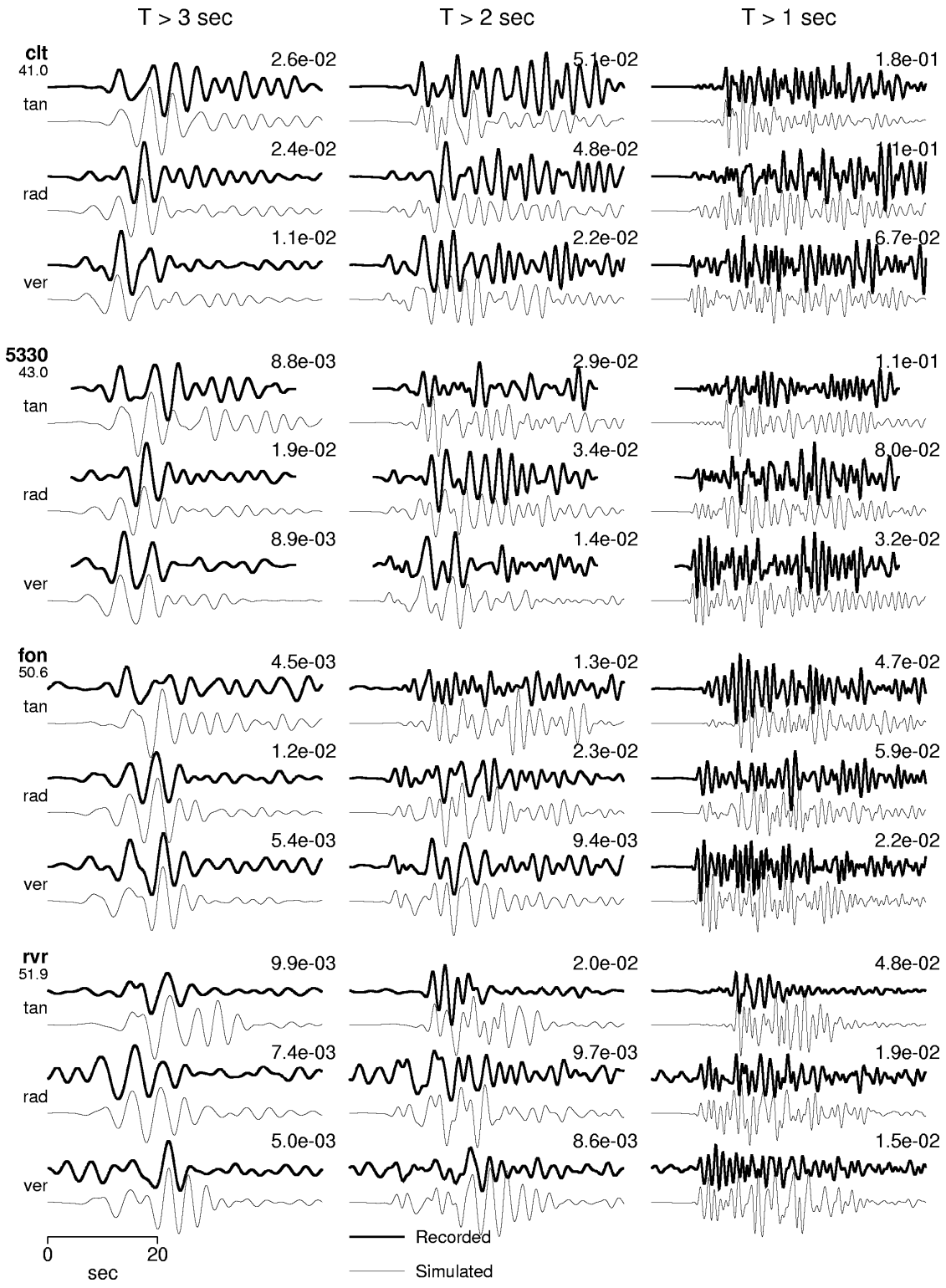
T > 3 sec
T > 2 sec
T > 1 sec
clt
41.0
tan
rad
ver
2.6e-02
5.1e-02
1.8e-01
2.4e-02
4.8e-02
1.1e-01
1.1e-02
2.2e-02
6.7e-02
5330
43.0
8.8e-03
2.9e-02
1.1e-01
1.9e-02
3.4e-02
8.0e-02
8.9e-03
1.4e-02
3.2e-02
fon
50.6
4.5e-03
1.3e-02
4.7e-02
1.2e-02
2.3e-02
5.9e-02
5.4e-03
9.4e-03
2.2e-02
rvr
51.9
9.9e-03
2.0e-02
4.8e-02
7.4e-03
9.7e-03
1.9e-02
5.0e-03
8.6e-03
1.5e-02
0
20
sec
Recorded
Simulated

Figure 9d.

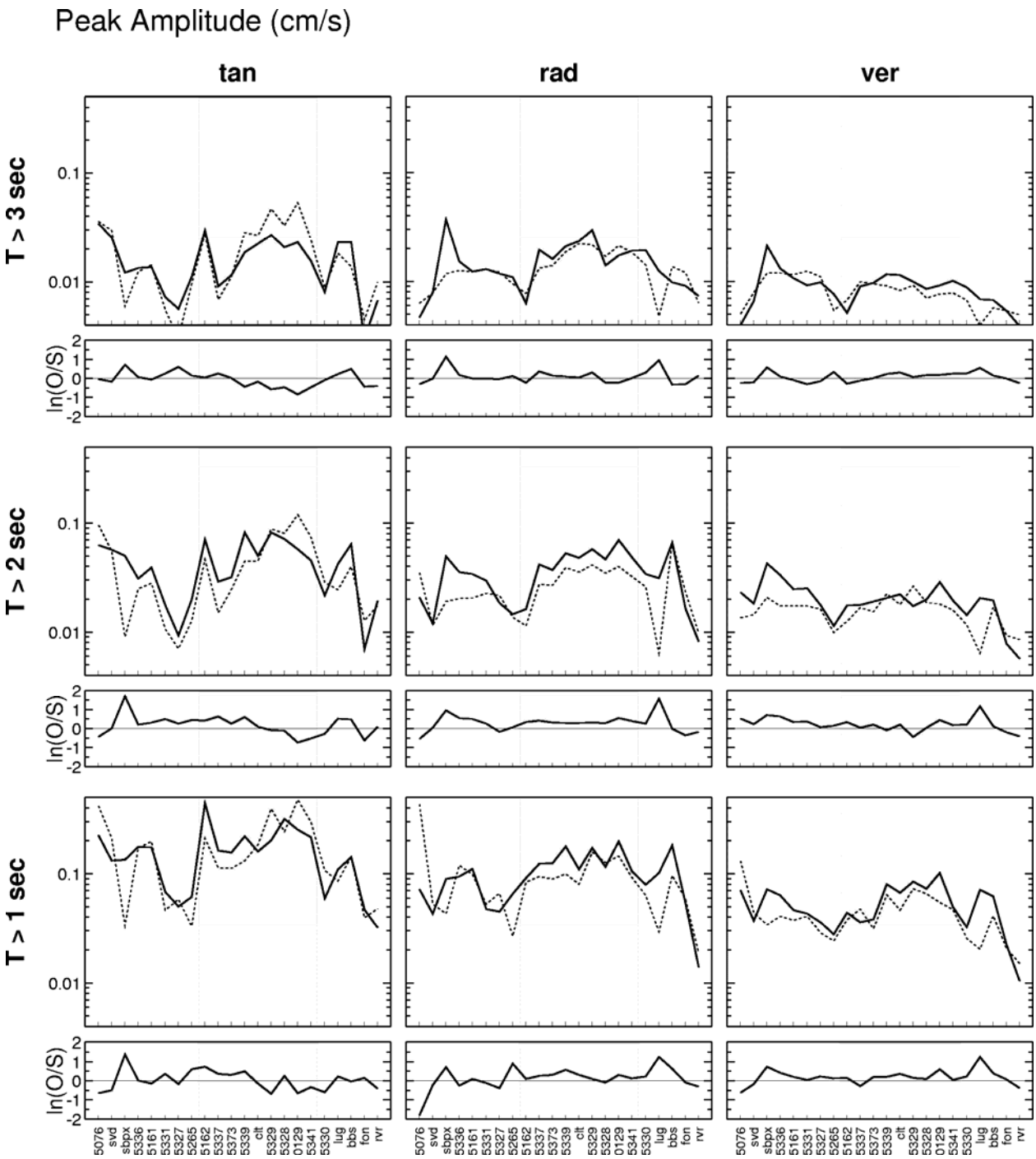
Peak Amplitude (cm/s)
tan
rad
ver
T > 3 sec
T > 2 sec
T > 1 sec
0.1
0.01
ln(O/S)
2
1
0
-1
-2
5076
svd
sbpx
5336
5161
5331
5327
5265
5162
5337
5373
5339
clt
5329
5328
0129
5341
5330
lug
bbs
fon
rvr

Figure 10.

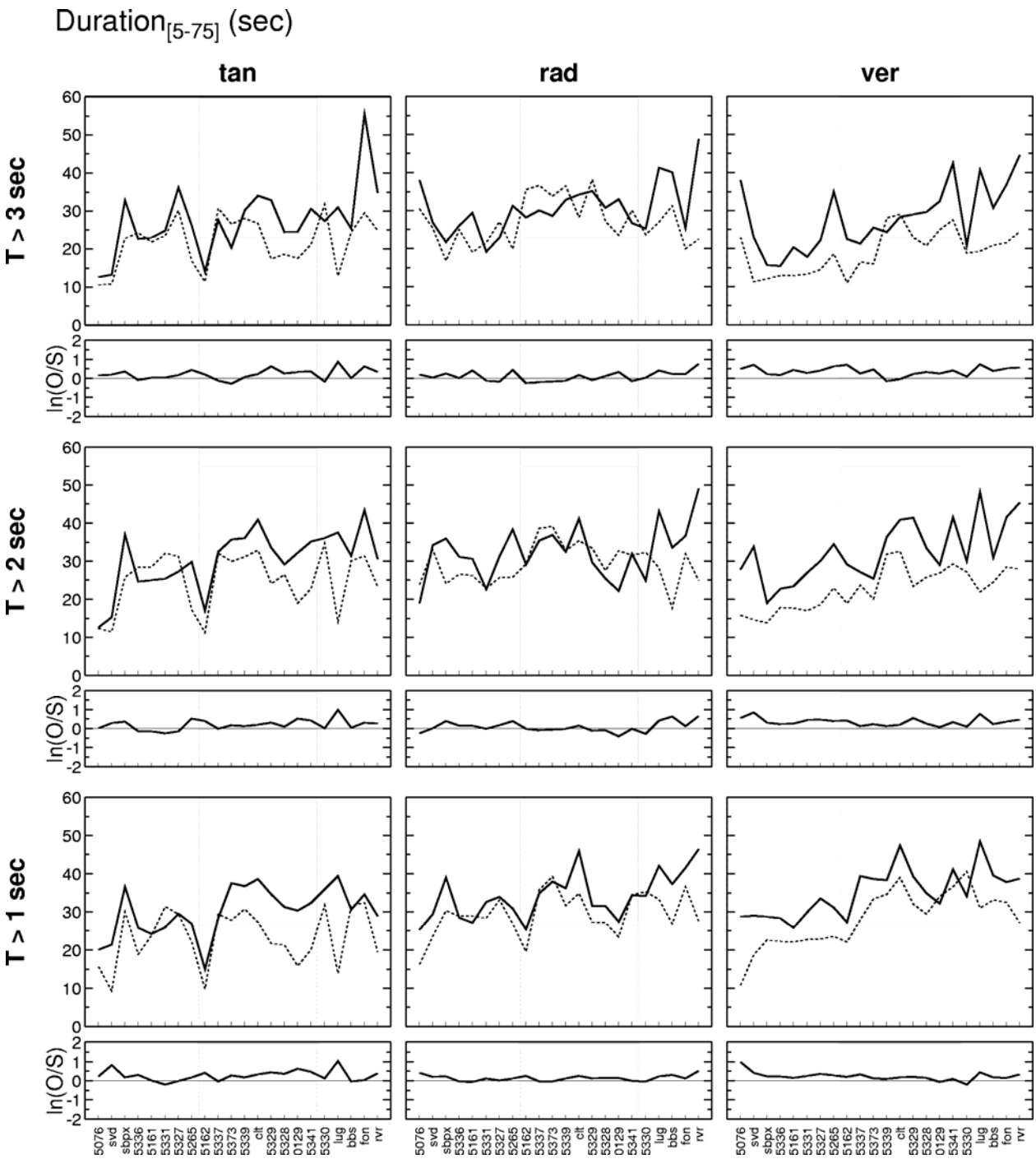
Duration[5-75] (sec)
tan
rad
ver
T > 3 sec
T > 2 sec
T > 1 sec
ln(O/S)
5076
svd
sbpx
5336
5161
5331
5327
5265
5162
5337
5373
5339
clt
5329
5328
0129
5341
5330
lug
bbs
fon
rvr

Figure 11.

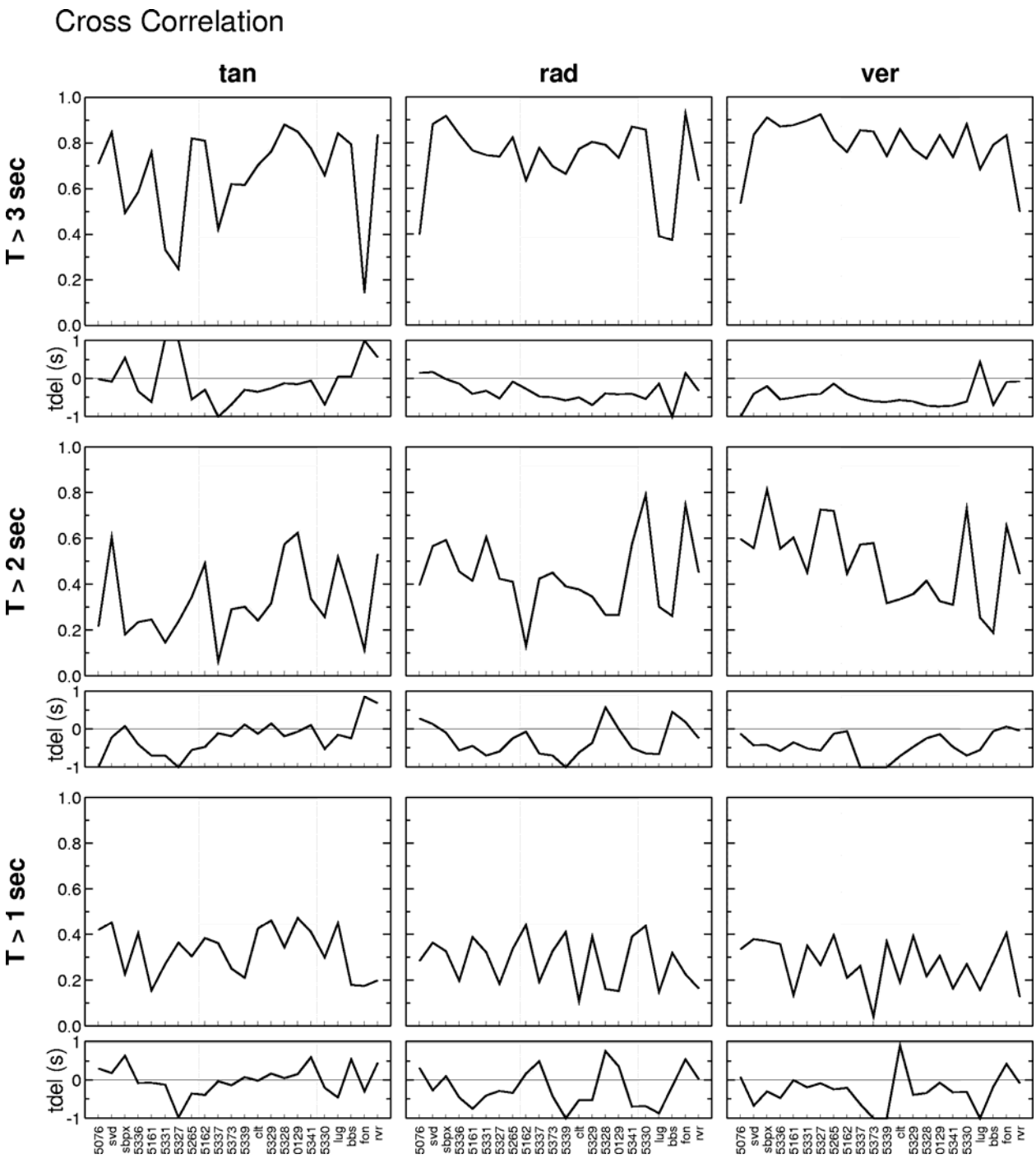
Cross Correlation
tan
rad
ver
T > 3 sec
T > 2 sec
T > 1 sec
tdel (s)
5076
svd
sbpx
5336
5161
5331
5327
5265
5162
5337
5373
5339
clt
5329
5328
0129
5341
5330
lug
bbs
fon
rvr

Figure 12.

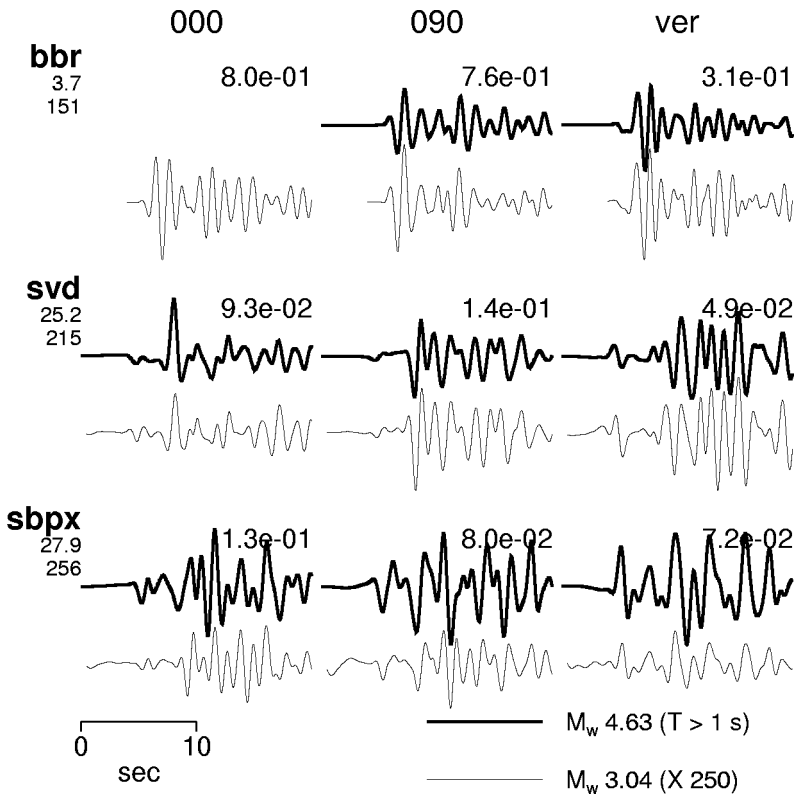
000
090
ver
bbr
3.7
151
8.0e-01
7.6e-01
3.1e-01
svd
25.2
215
9.3e-02
1.4e-01
4.9e-02
sbpx
27.9
256
1.3e-01
8.0e-02
7.2e-02
0
10
sec
Mw 4.63 (T > 1 s)
Mw 3.04 (X 250)

Figure 13.